Ion Sieving Effects in Chemically Tuned Pillared Graphene Materials for Electrochemical Capacitors

Harish Banda, Barbara Daffos, Sandy Périé, Yves Chenavier, Lionel Dubois, David Aradilla, Stephanie Pouget, Patrice Simon, Olivier Crosnier, Pierre-Louis Taberna, et al.

This is an author's version published in: **http://oatao.univ-toulouse.fr/21788**

Ion Sieving Effects in Chemically Tuned Pillared Graphene Materials for Electrochemical Capacitors

Harish Banda,[*,†] Barbara Daffos,[§,⊥] Sandy Périé,[†] Yves Chenavier,[†] Lionel Dubois,[†] David Aradilla,[†] Stéphanie Pouget,[‡] Patrice Simon,[§,⊥] Olivier Crosnier,[∥] Pierre-Louis Taberna,[§,⊥] and Florence Duclairoir[*,†]

[†]Univ. Grenoble Alpes, CEA, CNRS, INAC, SyMMES, Grenoble 38000, France
[‡]Univ. Grenoble Alpes, CEA, CNRS, INAC, MEM, Grenoble 38000, France
[§]CIRIMAT, Université de Toulouse, CNRS, INPT, UPS, 31062 Toulouse, France
[∥]Institut des matériaux Jean Rouxel (IMN), Univ. de Nantes, CNRS, Nantes 44300, France
[⊥]Réseau sur le Stockage Electrochimique de l'Energie (RS2E), FR CNRS 3459, Amiens 80039, France

ⓢ *Supporting Information*

ABSTRACT: Supercapacitors offer high power densities but require further improvements in energy densities for widespread commercial applications. In addition to the conventional strategy of using large surface area materials to enhance energy storage, recently, matching electrolyte ion sizes to material pore sizes has been shown to be particularly effective. However, synthesis and characterization of materials with precise pore sizes remain challenging. Herein, we propose to evaluate the layered structures in graphene derivatives as being analogous to pores and study the possibility of ion sieving. A class of pillared graphene based

materials with suitable interlayer separation were synthesized, readily characterized by X-ray diffraction, and tested in various electrolytes. Electrochemical results show that the interlayer galleries could indeed sieve electrolyte ions based on size constrictions: ions with naked sizes that are smaller than the interlayer separation access the galleries, whereas the larger ions are restricted. These first observations of ion sieving in pillared graphene-based materials enable efficient charge storage through optimization of the *d*-spacing/ion size couple.
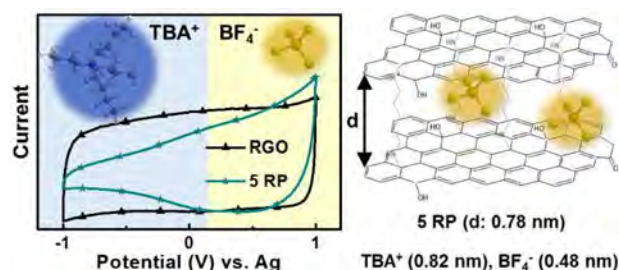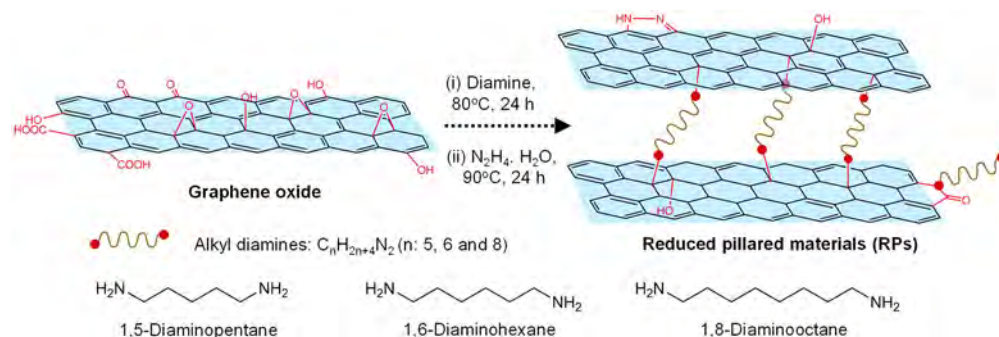
INTRODUCTION

Electrical double-layer capacitors, commonly known as supercapacitors (SCs), store energy through reversible adsorption of electrolytic ions on the charged electrode surfaces.[1] The non-faradaic nature of this charge storage enables supercapacitors to have high power densities and long cycle lives.[2] As an undesired consequence, non-faradaic charge storage also results in typically low energy densities in SCs.[3] Hence, porous carbon materials [e.g., activated carbons (ACs) and templated carbons] with large specific surface areas (SSAs) and good electrical conductivities are typically studied as electrode materials for improved energy densities.[4,5] However, the traditional beliefs about the large surface area of the material being a unique strategy for maximized charge storage needed to be reconsidered when complementary storage mechanisms were discovered in nanopores (<1 nm).[6] Following the work by Aurbach et al. on selective electrosorption of ions based on size (ion sieving),[7] researchers have reported the capacitance contribution from these nanopores in SCs.[8,9] Extensive work on carbide-derived carbons (CDCs)[10] and ACs has since revealed that the nanopores offer more efficient charge storage by confining the electrolytic ions and thereby restricting excessive charge screening by solvent molecules.[4,11] These

studies also revealed that the ions access such narrow pores by shedding a part of their solvation spheres.[12,13] Recent studies using Electrochemical Quartz Crystal Microbalance (EQCM)[14] and Nuclear Magnetic Resonance (NMR) techniques have quantitatively confirmed such desolvation.[15,16]

Several reports have since studied charge storage in nanopores and proposed that the maximum specific capacitances are obtained when ion sizes and pore sizes match.[17,18] In particular, it was also shown that a narrow pore size distribution (PSD) of a carbon material is essential for such observations.[19] However, only a few carbons, such as CDCs and some ACs, display narrow PSDs.[4] Furthermore, reliable determination of PSDs from gas adsorption studies remains difficult as the density functional theory-based approaches require prior knowledge of the pore geometry and heat of adsorption of the material.[4] To that end, combinations of characterization and modeling techniques using NMR and small-angle X-ray scattering are being used to allow unambiguous pore size and geometry determination.[20−22] In parallel, research on graphene

Scheme 1. Representation for the Synthesis of RPs[a]

Graphene oxide

(i) Diamine, 80°C, 24 h

(ii) N₂H₄. H₂O, 90°C, 24 h

Reduced pillared materials (RPs)

Alkyl diamines: $C_nH_{2n+4}N_2$ (n: 5, 6 and 8)

H_2N — NH_2 1,5-Diaminopentane

H_2N — NH_2 1,6-Diaminohexane

H_2N — NH_2 1,8-Diaminooctane

[a]For the sake of simplicity, the materials are depicted with single graphene sheets.
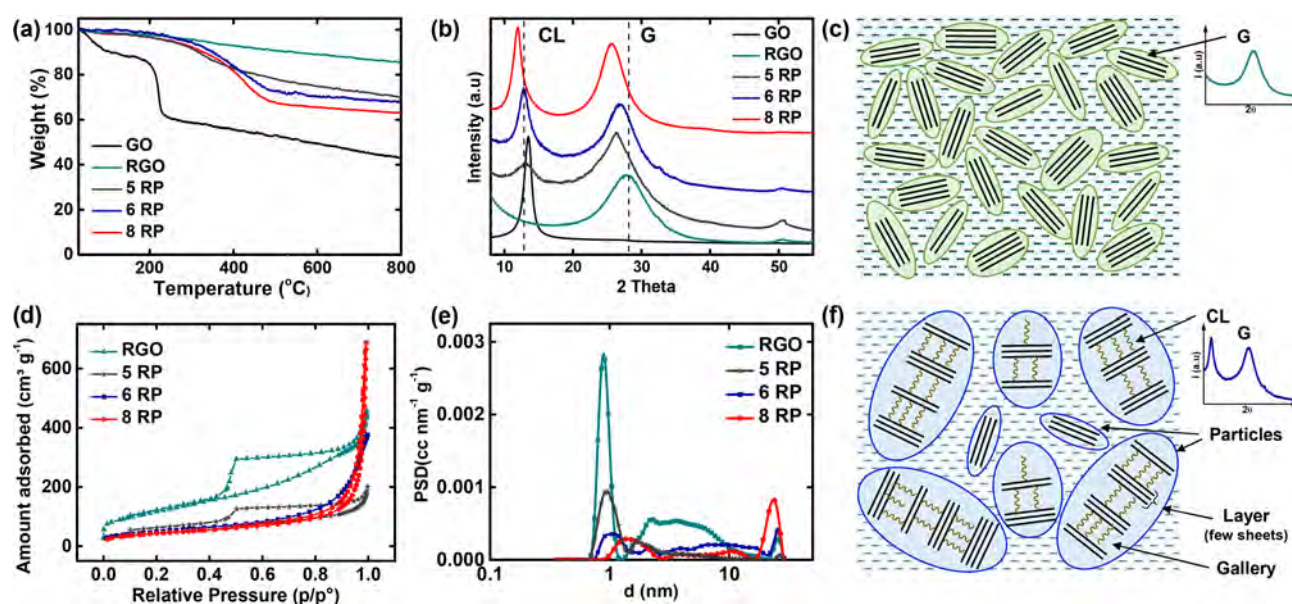

Figure 1. (a) Thermogravimetric analyses (50 °C/min) under a N₂ atmosphere and (b) X-ray diffraction patterns of the synthesized materials. The two different regions in XRD are attributed to graphitic (G) and cross-linked (CL) domains. (c) RGO is schematically represented with the G domain, and (f) 6 RP is shown with both G and CL domains. (d) N₂ sorption isotherms recorded at 77 K and (e) pore size distributions calculated using nonlocal density functional theory for RGO and RPs.

derivatives for SCs has shown potential in their large surface areas, electrical conductivities, and mechanical flexibilities.[23,24] However, in the context of material porosity for charge storage, much of the current research in graphene derivatives is devoted to improving the morphology with a focus on interparticle porosity,[25] similar to the research on ACs. Surprisingly, little attention has been devoted to exploring the unique layered structures of graphene derivatives in SCs. Although the natural graphitic spacing of 0.33 nm, defined as the intrinsic intraparticular pore, could be narrow for some ions in SCs, graphene derivatives are known to exhibit expanded layered structures (extrinsic intraparticular pores).[26] These expanded layered structures could be precisely tuned, and the *d*-spacing values describing interlayer distances could readily be evaluated using X-ray diffraction (XRD). Recent study of electrochemically exfoliated graphene oxide (GO) films showed enhanced capacitances when the *d*-spacing matched the ion sizes. This *in situ* study offers a proof of concept for the impact of *d*-spacing in SCs, but the low capacitance values of ∼1 F g⁻¹ mandate further improvements.[27] Few other reports have studied pillared graphene based materials in SCs, but the enhanced

performances could be related to only the improved hierarchical porosity.[28,29]

In this context, herein, we study the electrosorption of ions in pillared graphene materials with varied interlayer distances. An analysis of such materials would test the possibility of ion sieving and, thereby, ion confinement in the interlayer galleries for efficient charge storage. A class of materials using GO as a precursor and alkyl diamines as covalent pillars were synthesized and then chemically reduced to yield suitable electrical and morphological characteristics for SCs. XRD patterns of the synthesized materials gave evidence of the expanded structures with determination of the respective *d*-spacing values. Extensive electrochemical characterization was performed in SCs using electrolytes containing constant anion but varied cation sizes. The observed electrochemical responses clearly show limitations in ion adsorption based on size constrictions, and a direct correlation between *d*-spacing values and ion sizes was noted. These first results for ion sieving in pillared graphene materials could help us readily design and develop materials for optimized charge storage in SCs.

■ MATERIALS AND CHARACTERIZATION

Material Design. GO has long been studied as a perfect precursor for various graphene-like materials, because of its surface functionalities that offer abundant chemical tenability.[30] GO is characterized with randomly distributed oxygen-containing functional groups, and it is believed that the epoxy and hydroxyl groups lie above and below each layer whereas the carboxylic groups are on the edges.[31] This rich surface chemistry allows covalent bonding of GO sheets with an organic linker. In particular, a bifunctional linker bearing its reactive functions at both ends is used to cross-link two sheets together.[32] For example, alkyl diamines, very reactive toward epoxide groups, have been shown to be effective in forming pillared materials with tunable interlayer distances.[32,33] Hence, we use diamines with varied alkyl chain lengths (5, 6, and 8) to obtain the necessary *d*-spacing values for this study. GO is electrically insulating, and reaction with the alkyl diamines could not ensure sufficiently high electrical conductivities of these pillared materials.[34] The obtained materials are thus chemically reduced using hydrazine to synthesize reduced pillared materials (RPs). Depending on the diamine used in the first step, RPs are named 5 RP (1,5-diaminopentane), 6 RP (1,6-diaminohexane), and 8 RP (1,8-diaminooctane) (Scheme 1). As a control, reduced graphene oxide (RGO) is also made by reduction of GO. Notably, as the GO precursor is not specifically treated to obtain single GO sheets, it is likely that each graphene layer in the synthesized materials consists of a few sheets rather than a single graphene sheet.

Experimental Section. GO synthesis was achieved through a modified Hummers and Offeman's method.[42,43] An aqueous solution of well-dispersed 5 mg/mL GO was prepared and used as a precursor for further syntheses. The initial synthesis of pillared materials, named Ps, involves a straightforward reaction between various diamines and GO solution (Scheme 1). 5 P, 6 P, and 8 P were synthesized using 1,5-diaminopentane, 1,6-diaminohexane, and 1,8-diaminooctane, respectively. At first, 150 mL of a GO solution and 57 mmol of each diamine were mixed and sonicated for 10 min. The mixtures were then heated at 80 °C for 24 h while being continuously stirred. The reaction mixtures were then filtered, cleaned with an excess of water and ethanol, and dried overnight under a vacuum at 100 °C. The obtained pillared materials were further reduced by being treated with an excess of hydrazine hydrate at 90 °C for 24 h while being continuously stirred. The obtained reduced pillared materials were cleaned with an excess of water, dried under a vacuum at 100 °C, and labeled as the respective RPs (5 RP, 6 RP, and 8 RP). As a control to the RPs, RGO was also synthesized by treating GO with hydrazine hydrate. For reliable comparisons, the two-step protocol described above was followed for RGO, as well.

Characterization. The physicochemical properties of the synthesized materials were characterized using various techniques, and the porosity characteristics were analyzed using scanning electron microscopy (SEM) and gas sorption studies. The thermal degradation responses of the materials were obtained using thermogravimetric analysis (TGA) and are shown in Figure 1a. Consistent with previous reports,[30,35] GO displays a two-step weight loss profile with the first removal of the adsorbed water occurring below 100 °C and an abrupt weight loss around 200 °C corresponding to decomposition of surface oxygen functional groups. Additionally, a steady loss beyond 200 °C is also seen because of the gradual removal of stable functionalities. Upon reaction of GO with hydrazine, the abrupt weight loss and moisture removal are no longer seen, suggesting an efficient chemical reduction. Synthesized via a two-step process, RPs also show no removal of moisture or oxygen functionalities but exhibit a gradual weight loss between 300 and 500 °C. Such gradual weight losses at temperatures above the boiling points of the respective diamines are attributed to the removal of nonlabile diamine species.[35] Hence, TGA shows the presence of diamine linkers and an absence of labile oxygen functional groups in RPs. Furthermore, a careful analysis of the weight losses identifies similar diamine grafting densities in all three RPs (Table S1).

X-ray photoelectron spectroscopy (XPS) was performed to analyze the surface elemental composition of the synthesized materials. The

survey spectra of the materials indicate the presence of C, N, and O elements, with GO showing O intensities significantly higher than and N intensities significantly lower than others (Figure S1a). High-resolution C 1s spectra of the materials show two main peaks at 284.5 and 286.5 eV for GO, whereas RGO and RPs have a single main peak at 284.5 eV (Figure S1b). The observed C 1s signals were deconvoluted and assigned as C=C/C−C (284.5 eV), C−OH (285.9 eV), alkoxy/epoxy (286.5 eV), and carbonyl components (288.3 eV) based on earlier reports (Figure S2).[30] GO exhibits a highly oxidized nature in the presence of various oxygen-containing functional groups and the predominant peak corresponding to alkoxy/epoxy groups; on the other hand, RGO and RPs show a significant decrease in oxygen functionalities, and the predominant peak is assigned to C=C/C−C. In addition, a new peak at 285.6 eV corresponding to C−N was observed. The surface elemental compositions obtained from survey spectra show a decrease in O content from 26% in GO to 4−8% in RGO and RPs with an additional incorporation of 4−6% N. These observations indicate efficient reduction of oxygen functionalities and incorporation of N groups into RGO and RPs. High-resolution N 1s spectra reveal a very weak signal for GO and clear peaks, with varied positions, for RGO and RPs (Figure S3). Deconvolution of N signal could explain this shift in peak positions and the differences in N content between RGO and RPs. As evoked in the literature, the diamines could react and form covalent linkages with GO, resulting in amine N (399.2 eV), and instigate further internal rearrangements forming pyridinic (398.2 eV), pyrrolic (400.2 eV), and graphitic N (401.5 eV) components.[35] RGO shows a typical abundance of N in pyrrolic and graphitic rings because of the strong reducing nature of hydrazine, whereas RPs have a major contribution from amine N, owing to the incorporation of diamines, and thus show a shift in the peak position compared to that of RGO. These results reaffirm the presence of covalently linked diamines in RPs as also seen via TGA.

XRD patterns were obtained to directly analyze the layered structures of the synthesized materials (Figure 1b). Freeze-dried GO shows a sharp peak at 13.5° related to a *d*-spacing of 7.6 Å, indicating a high degree of oxidation in the starting material. RGO displays a broad peak at 28° corresponding to a graphite-like pattern (002), suggesting partial restacking of graphene sheets due to the removal of oxygen functionalities during chemical reduction. Synthesized in a two-step process, RPs exhibit diffraction patterns with two distinct peaks around 25−27° and 11−13° each. The broad peaks at larger angles correspond to graphite-like partial restacking and indicate a degree of reduction close to that of RGO. The relatively sharper peaks at smaller angles show a gradual increase in *d*-spacing from 7.8 Å (5 RP), 8.0 Å (6 RP), to 8.6 Å (8 RP) with increasing lengths of diamines used. Earlier studies have attributed these peaks to the expanded layered structures caused by intercalation of diamines between the graphene layers.[32] Although the *d*-spacing values relate to the diamines used, an exact prediction of *d*-spacing based on alkyl chain lengths is difficult to obtain as it requires knowledge of the local orientation and conformation of diamines.[32] Additionally, the increased *d*-spacing values demonstrate intercalation of the linker between the graphene layers but do not confirm their covalent cross-linking. Swelling experiments were proposed in the literature as an indirect way to analyze the cross-linking of the graphene layers.[32,33] If the RPs were covalently linked by the diamine, they should resist swelling by solvents. XRD patterns of 8 RP after it had been soaked overnight in an ethanol/water solution remain unchanged and confirm that the intercalated diamine indeed covalently cross-links the layers (FigureS4a) as already suggested by TGA and XPS. In a parallel test with GO (Figure S4b), visible swelling and a shift in XRD peak positions are seen just after a few minutes in the solvent, thus highlighting the lack of cross-linking.

In summary, the synthesized materials could possess two different domains corresponding to graphitic-like (G) and cross-linked (CL) arrangements. The G domains are attributed to partially stacked graphene sheets with a *d*-spacing of ∼3.5−4.0 Å, whereas CL domains relate to cross-linked graphene layers and are characterized by *d*-spacing values of 7.8−8.6 Å. RGO, synthesized as a control material,
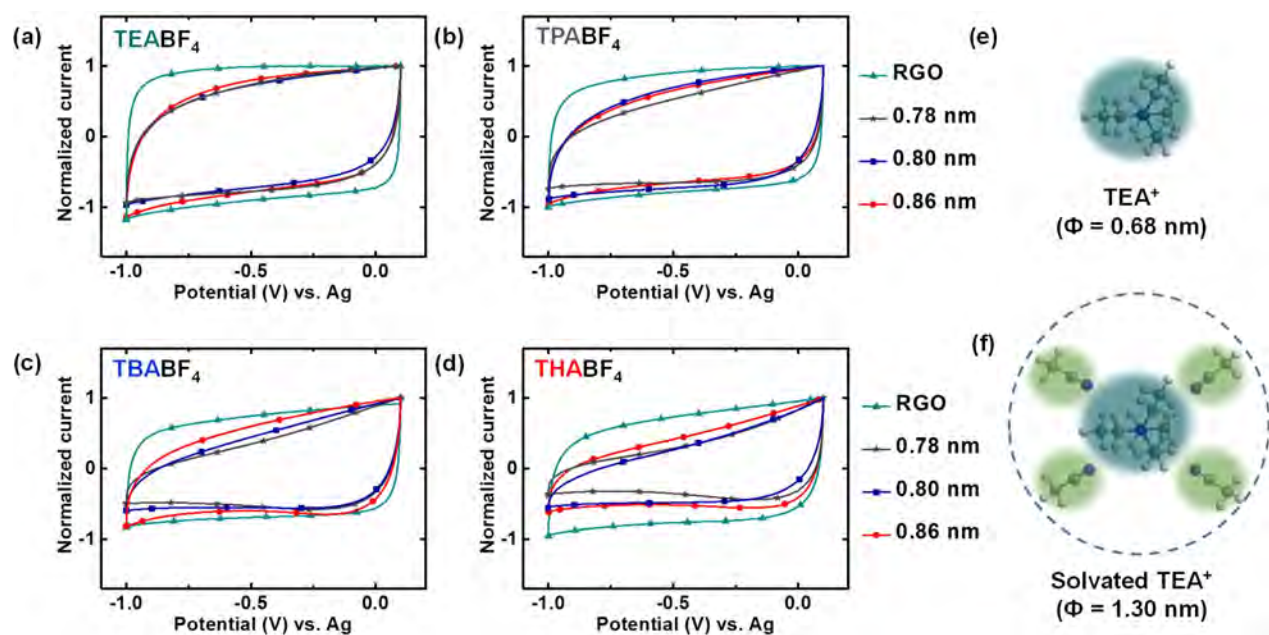
Figure 2. Normalized CVs of RGO and RPs obtained at a scan rate of 20 mV s^{-1} in the voltage range of 0.1 to -1.0 V vs Ag using 1 M solutions of (a) TEABF$_4$ (Φ = 0.68 nm), (b) TPABF$_4$ (Φ = 0.76 nm), (c) TBABF$_4$ (Φ = 0.82 nm), and (d) THABF$_4$ (Φ = 0.95 nm) in acetonitrile as electrolytes. (e and f) Naked and solvated TEA$^+$ species and their diameters, respectively. The chosen voltage window maintains negative polarization in the materials and ensures adsorption and desorption of mainly the cation.

has only the G stacking of the sheets (Figure 1c), whereas RPs have both G and CL domains coexisting in a random manner (Figure 1f). Additionally, the CL peaks in RPs could be seen to become narrow from 5 RP to 8 RP when larger diamines are used (Figure 1b). These sharper peaks with increased alkyl chain lengths probably arise from improved flexibilities of diamines that enable formation of larger particles. Hence, the CL peaks in XRD patterns evidence formation of expanded layered structures and also suggest varied particle sizes between RPs.

SEM images show a porous morphology for RGO and RPs without any obvious differences (Figure S5). The observed morphologies were then analyzed by N$_2$ sorption isotherms recorded at 77 K, and the SSA and PSDs were obtained using two-dimensional nonlocal density functional theory (NLDFT)[36,37] (details in the Supporting Information). The synthesized materials exhibit type II adsorption−desorption behavior with a hysteresis loop indicating the presence of micro- and mesopores (Figure 1d).[29] RGO has the largest SSA of 330 m^2 g^{-1}, whereas RPs display lower SSA values, with values decreasing from 138 m^2 g^{-1} in 5 RP to 130 m^2 g^{-1} in 6 RP and 108 m^2 g^{-1} in 8 RP (Table S1). There are two plausible reasons that the observed surface areas of RPs are smaller than those of RGO: (i) diamines increase the overall inactive weight of RPs, and (ii) the diamine pillars may sterically hinder the gas sorption and the interlayer gallery pores are rendered as closed pores.[38] If the interlayer galleries indeed act as closed pores, surfaces of the graphene layers in the CL arrangement would be inaccessible and result in such lower SSA values. The calculated PSDs show significant contributions from micropores and the presence of mesopores in RGO, whereas the PSDs for RPs vary with the diamine used (Figure 1e and Figure S6). All RPs possess both types of pores, but with increasing chain lengths, the micropore content decreases and the mesopore content increases. This could be explained by the XRD patterns that suggested larger particle sizes in RPs with larger diamines resulting in such mesoporosity.

The characterization techniques mentioned above describe RPs as being reduced, covalently linked, and morphologically suitable for application in SCs. TGA, XRD, and XPS showed the presence of diamines, while the swelling experiments provide evidence of cross-linking. SEM and gas sorption analyses attribute a porous morphology to RPs, and the PSD curves indicate the predominant presence of >1 nm pores with little or no contribution from smaller pores. The dearth

of such nanopores highlights RPs as ideal materials for studying the distinct impact of interlayer galleries on SC performance. Furthermore, the cross-linked galleries have *d*-spacing values in the range of sizes for the commonly used electrolyte ions and thus offer a good template for studies in SCs.

■ ELECTROCHEMICAL STUDIES

The ion sieving behavior of these reduced pillared graphene materials was studied in SCs by using a range of electrolytes with varying ion sizes. Tetraalkylammonium tetrafluoroborate (TAABF$_4$) salt solutions (1 M) in acetonitrile with a constant anion size and varying cation sizes [ethyl (TEA$^+$, 0.68 nm), propyl (TPA$^+$, 0.76 nm), butyl (TBA$^+$, 0.82 nm), and hexyl (THA$^+$, 0.95 nm)][39] were used as electrolytes. A three-electrode configuration in SCs was adapted to study the individual electrode responses. Cyclic voltammograms (CVs) were acquired by scanning the cells from open-circuit potential (OCV ∼ 0.1 V) to positive and negative terminal potentials separately to record the distinct anion and cation sorption responses. For ease of comparison, all CVs are normalized with the respective currents at 0.1 V versus Ag and the curves are denoted with their respective *d*-spacing values: 0.78 nm for 5 RP, 0.80 nm for 6 RP, and 0.86 nm for 8 RP.

Figure 2 shows the CVs obtained for RGO and RPs in various TAABF$_4$ electrolytes at a scan rate of 20 mV s^{-1} in the potential range from -1.0 to 0.1 V versus Ag. These scans from OCV to negative potentials mainly relate to the adsorption/desorption responses of TAA$^+$ cations. When tested with the TEABF$_4$ electrolyte (Figure 2a), all the materials showed nearly rectangular curves with no specific features suggesting an ideal double-layer charge storage mechanism. Upon using a slightly larger cation with the TPABF$_4$ electrolyte (Figure 2b), the CV curves of the materials remain comparable except for that of 5 RP, which indicates a slight reduction in current at the negative terminal potential. When we move to an even larger cation in TBABF$_4$, both 5 RP and 6 RP show a steep reduction in current
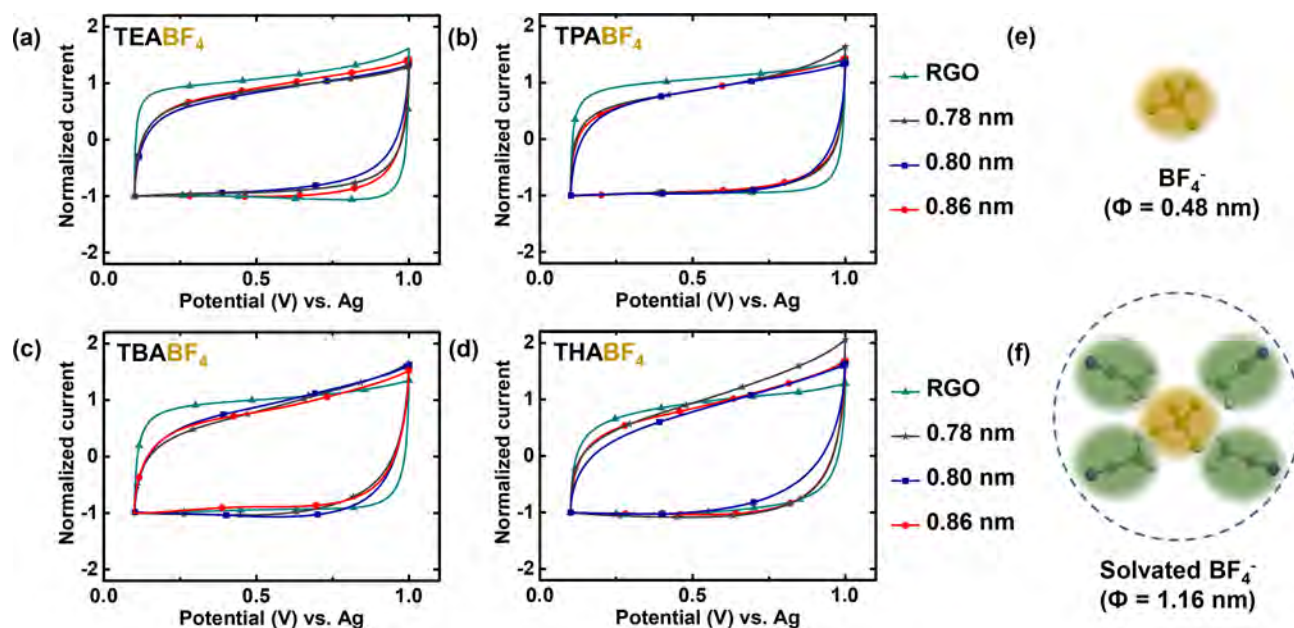
Figure 3. Normalized CVs of RGO and RPs obtained at a scan rate of 20 mV s^{-1} in the voltage range of 0.1−1.0 V vs Ag using 1 M solutions of (a) TEABF$_4$, (b) TPABF$_4$, (c) TBABF$_4$, and (d) THABF$_4$ in acetonitrile as electrolytes. (e and f) Naked and solvated BF$_4^-$ species and their diameters, respectively. The chosen voltage window maintains positive polarization in the materials and ensures adsorption and desorption of mainly the anion.

at lower potentials whereas 8 RP remains mostly unchanged (Figure 2c). Finally, when the largest cation is tested using THABF$_4$, all the RPs display significantly decreased currents (Figure 2d). Moreover, the asymmetric shapes of CVs indicate that these limitations in currents at negative terminal potentials are not consequences of poor electrical or ionic conductivities. In turn, the behavior of RGO remains nearly unchanged regardless of the electrolyte used. These behaviors for RGO and RPs were also observed when CVs were recorded at scan rates of 10 and 50 mV s^{-1}. The data given above clearly suggest an explicit dependence of electrochemical responses from RPs based on the size of cations used. This tunable ion accessibility in RPs highlights them as sufficiently rigid layered structures that can restrict ions that are larger than the *d*-spacing. As already evidenced by TGA, XPS, and XRD, covalent interaction between graphene and diamines is likely to be responsible for this electrochemical behavior.

Studies of CDCs have noted such reductions in currents, i.e., the limitations in ion adsorption, when the naked electrolyte ions are larger than the average pore sizes.[11] In the study presented here, though we observe a similar ion limitation, gas sorption results have indicated a dearth of pores that are smaller than the cations tested. However, as evoked earlier, the gas sorption studies may deem the interlayer gallery pores in RPs as closed pores that, nevertheless, could be accessible to ion adsorption under polarization. Hence, the *d*-spacing values of RPs were directly compared with the naked ion sizes by plotting the electrochemical data as responses for each material (Figure S7). 5 RP, with a *d*-spacing of 0.78 nm, shows a regular CV in TEA$^+$ (0.68 nm), but an increasing limitation in ion adsorption is seen from TPA$^+$ (0.76 nm) to THA$^+$ (0.95 nm). 6 RP is characterized by a *d*-spacing of 0.80 nm, and it allows TEA$^+$ or TPA$^+$ but limits TBA$^+$ and THA$^+$ cations. 8 RP behaves similarly by limiting THA$^+$ that is larger than its *d*-spacing of 0.86 nm. These observations clearly show that the cations are limited in RPs when the naked ion sizes are larger than the interlayer distances. Conversely, the cations enter the

gallery pores of RPs when their naked ion sizes are smaller (Figure 2e). Meanwhile, RGO shows no limitations indicating that ion adsorption occurs only in the interparticle porosity. Additionally, RGO shows perfect rectangular curves compared to those of RPs probably because of its superior electrical and ionic conductivities owing to a lack of diamine residues.[35]

The electrosorption behavior of BF$_4^-$ anions was analyzed by performing CVs in the positive voltage window from 0.1 to 1.0 V versus Ag (Figure 3). Unlike the behavior under negative polarization, RGO and RPs both show nearly rectangular curves in all the electrolytes indicating no limitation for the BF$_4^-$ anion. Similar results were recorded when CVs were acquired at scan rates of 10 and 50 mV s^{-1}. CVs were then recorded in the full potential window of −1.0 to 1.0 V versus Ag and were shown to correspond to the behavior of each material in different electrolytes (Figures S8 and S9). RGO shows identical half-curves on both sides of the OCV, suggesting no specific difference for TAA$^+$ or BF$_4^-$ adsorption (Figure S8a). RPs also display identical half-curves when both naked ion sizes are smaller than the *d*-spacing values, but if the cation size is larger, a clear distinction could be seen between the two halves of a CV. For instance, 6 RP shows an ideal CV curve with TEABF$_4$, but distinct anion and cation adsorptions are seen in TBABF$_4$ and THABF$_4$ electrolytes (Figure S8c). The naked BF$_4^-$ anion is smaller than the cross-linked galleries in RPs (Figure 3e) and is not limited; on the other hand, the TAA$^+$ cations vary in size from 0.68 to 0.95 nm, and their adsorptions are limited by size constrictions. Hence, these observations confirm that the interlayer galleries in pillared graphene materials indeed sieve ions on the basis of sizes. Furthermore, the durability of the diamine pillars was tested by cycling 8 RP in THABF$_4$ electrolyte (Figure S10). CVs at the 50th and 500th cycles show identical limitation for THA$^+$ cations, and the XRD patterns for the electrode before and after cycling remain similar (Figure S10b,c). In particular, the presence of the CL peak around 12° before and after cycling confirms the retention of the pillars. Besides the characterization conducted on the
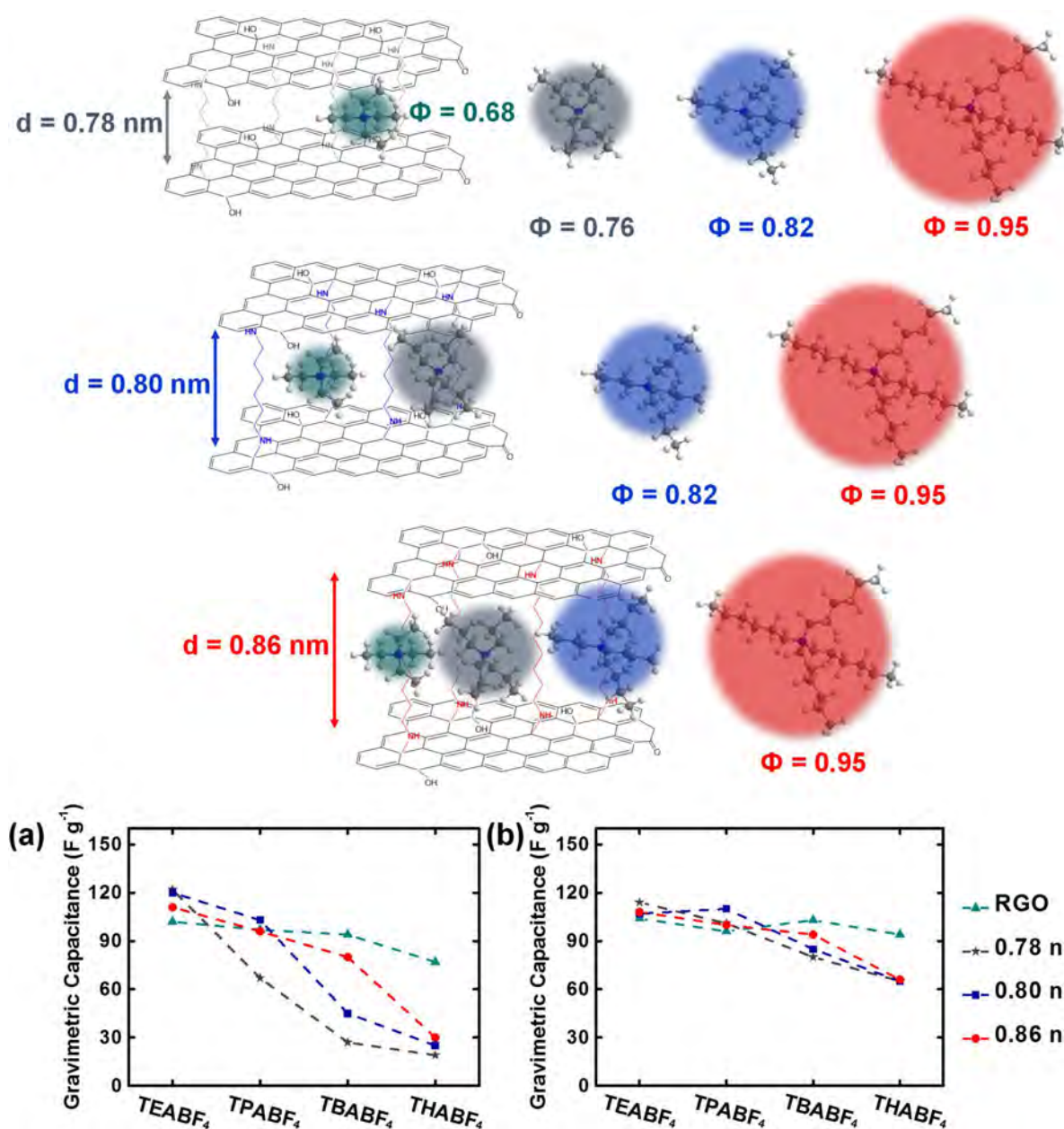
Figure 4. Schematic representation showing the limitation of TAA$^+$ cations moving into RPs based on size constrictions. For the sake of simplicity, RPs are shown as individual graphene sheets cross-linked together instead of layers of graphene sheets bridged together. Specific capacitances are calculated from CVs at a scan rate of 20 mV s^{-1} for the cells tested in voltage ranges of (a) −1.0 to 0.1 V vs Ag and (b) 0.1 to 1.0 V vs Ag. Dashed lines are added as guides to the eye.

material, these electrochemical analyses performed under the influence of polarization provide additional proof of the successful covalent anchoring of the diamine on graphene. Otherwise, if the diamines were rather held by noncovalent interactions, polarization of the electrodes during cycling would lead to their release and to a structural change.

The direct relation between the naked ions and the *d*-spacing values of RPs raises interesting questions about the ion adsorption in gallery pores. Typically, an ion exists as a solvated species in a solution, and the solvation number, thus the solvated radii, depends on its interactions with the solvent.[11] In the study presented here, all the solvated TAA$^+$ (TEA$^+$, 1.30 nm) and BF$_4^-$ (BF$_4^-$, 1.16 nm) ions are larger than the interlayer distances in RPs, and thus, they could access the gallery pores only by partially shedding their solvation shells

(Figures 2f and 3f). In fact, earlier work on porous carbons has shown that the solvated electrolyte ions indeed enter smaller pores as partially desolvated ions.[15] Herein, we suggest a similar partial desolvation for ions in the gallery pores of RPs. However, advanced characterization using EQCM and NMR techniques is required to quantitatively confirm this partial desolvation.

Specific capacitances of RPs were calculated for both the anion and cation adsorption from CVs at a scan rate of 20 mV s^{-1} (Figure 4). For the cation adsorption, RGO exhibits close capacitance values around 100 F g^{-1} in all four electrolytes, underlining similar accessible electrochemical surface areas (Figure 4a). In turn, RPs show comparable capacitances around 120 F g^{-1} in TEABF$_4$ and exhibit lower capacitances when the cations could no longer be adsorbed in the gallery pores. For

instance, 5 RP performs like other RPs in TEABF$_4$, but the capacitance of 5 RP in TPABF$_4$ steeply declines to fractional values in THABF$_4$. 6 RP and 8 RP possess larger d-spacing values and thus show a decline starting with TBABF$_4$ and THABF$_4$, respectively. Notably, even with this ion limitation in RPs, some charge will always be stored rather than none as the interparticle pores and the bulk porosity in the materials are still accessible for ion sorption. For anion adsorption, RGO shows similar capacitance values of ~100 F g^{-1} in the four electrolytes (Figure 4b). Because the anions are not limited, RPs also exhibit close values in each electrolyte with a general trend of lower capacitances from TEABF$_4$ to THABF$_4$ electrolytes. Furthermore, the specific capacitances obtained in the full voltage window of −1.0 to 1.0 V versus Ag mirror the results seen for cations (Figure S11). RPs, with one-third of SSAs compared to RGO, exhibit capacitances of ~130 F g^{-1} in TEABF$_4$, close to that of RGO, and emphasize that the gas sorption analyses do not probe interlayer gallery pores in RPs and hence underestimate the overall electrochemically active surface area available. In other electrolytes, RPs exhibit a decline in capacitance from TPABF$_4$ to THABF$_4$ as the cation limitation becomes increasingly substantial. The overall lower capacitances of RPs compared to those of RGO could also arise for a couple of reasons: the incorporated alkyl chains contribute to the 20% increase in weight in RPs, and RPs exhibit an interparticle micropore volume that is smaller than that of RGO.

This study brings to light the possibility of using pillared graphene materials as reference materials for ion sieving and electrochemical adsorption in the interlayer gallery pores of structured graphene materials. The combination of XRD, gas sorption, and electrochemical analyses allowed us to identify the electrochemically active porosity in these systems. Although the observed capacitances already occur in the range of that of RGO and the current literature[40,41] (Table S2), pillared materials offer tremendous possibilities for improvements in both power and energy densities. Strategies such as using RPs that are synthesized with a low density of pillars could improve ionic diffusion and simultaneously ensure both higher power and energy densities. Additionally, the conventional strategy of developing hierarchical porosity in addition to the interlayer galleries could also enhance ion accessibility and charge storage.

CONCLUSIONS

A class of reduced pillared graphene materials with tunable interlayer galleries were readily synthesized using alkyl diamines as cross-links. A family of tetraalkylammonium tetrafluoroborate salts with constant anion and varying cation sizes in acetonitrile were used as electrolytes in SCs. The observed electrochemical responses for RGO show no ion specific limitation suggesting that the ion sorption occurs only in the interparticle porosity, whereas RPs show limitations based on size constrictions indicating that the ions mainly adsorb in the interlayer gallery pores. Ions are limited if their naked sizes are larger than the d-spacing of RP and thus show that the interlayer galleries sieve ions on the basis of size. This direct correlation between naked ion size and gallery spacing suggests partial desolvation of the electrolyte ions during adsorption. Further experiments using different solvents and characterization techniques are being analyzed to understand this desolvation. These first results of ion sieving in pillared graphene materials could help us readily design and develop strategies for optimized charge storage in SCs.

AUTHOR INFORMATION

Corresponding Authors
*E-mail: harish.banda@cea.fr.
*E-mail: florence.duclairoir@cea.fr.
ORCID ⊙
Patrice Simon: 0000-0002-0461-8268
Florence Duclairoir: 0000-0003-0257-0501

REFERENCES

(1) Conway, B. E. *Electrochemical Supercapacitors: Scientific Fundamentals and Technological Applications*; Springer, 1999.
(2) Simon, P.; Gogotsi, Y. Materials for Electrochemical Capacitors. *Nat. Mater.* **2008**, 7, 845−854.
(3) Burke, A. R&D Considerations for the Performance and Application of Electrochemical Capacitors. *Electrochim. Acta* **2007**, 53, 1083−1091.
(4) Béguin, F.; Presser, V.; Balducci, A.; Frackowiak, E. Carbons and Electrolytes for Advanced Supercapacitors. *Adv. Mater.* **2014**, 26, 2219−2251.
(5) Zhang, L. L.; Zhao, X. S. Carbon-Based Materials as Supercapacitor Electrodes. *Chem. Soc. Rev.* **2009**, 38, 2520−2531.
(6) Chmiola, J.; Yushin, G.; Gogotsi, Y.; Portet, C.; Simon, P.; Taberna, P. L. Anomalous Increase in Carbon Capacitance at Pore Sizes Less Than 1 Nanometer. *Science* **2006**, 313, 1760−1763.
(7) Eliad, L.; Salitra, G.; Soffer, A.; Aurbach, D. Ion Sieving Effects in the Electrical Double Layer of Porous Carbon Electrodes: Estimating Effective Ion Size in Electrolytic Solutions. *J. Phys. Chem. B* **2001**, 105, 6880−6887.
(8) Vix-Guterl, C.; Frackowiak, E.; Jurewicz, K.; Friebe, M.; Parmentier, J.; Béguin, F. Electrochemical Energy Storage in Ordered Porous Carbon Materials. *Carbon* **2005**, 43, 1293−1302.
(9) Largeot, C.; Portet, C.; Chmiola, J.; Taberna, P.-L.; Gogotsi, Y.; Simon, P. Relation between the Ion Size and Pore Size for an Electric Double-Layer Capacitor. *J. Am. Chem. Soc.* **2008**, 130, 2730−2731.
(10) Presser, V.; Heon, M.; Gogotsi, Y. Carbide-Derived Carbons − From Porous Networks to Nanotubes and Graphene. *Adv. Funct. Mater.* **2011**, 21, 810−833.
(11) Chmiola, J.; Largeot, C.; Taberna, P.-L.; Simon, P.; Gogotsi, Y. Desolvation of Ions in Subnanometer Pores and Its Effect on Capacitance and Double-Layer Theory. *Angew. Chem., Int. Ed.* **2008**, 47, 3392−3395.
(12) Merlet, C.; Rotenberg, B.; Madden, P. A.; Taberna, P.-L.; Simon, P.; Gogotsi, Y.; Salanne, M. On the Molecular Origin of

Supercapacitance in Nanoporous Carbon Electrodes. *Nat. Mater.* **2012**, *11*, 306−310.

(13) Merlet, C.; Péan, C.; Rotenberg, B.; Madden, P. A.; Daffos, B.; Taberna, P.-L.; Simon, P.; Salanne, M. Highly Confined Ions Store Charge More Efficiently in Supercapacitors. *Nat. Commun.* **2013**, *4*, 3701−3707.

(14) Levi, M. D.; Salitra, G.; Levy, N.; Aurbach, D.; Maier, J. Application of a Quartz-Crystal Microbalance to Measure Ionic Fluxes in Microporous Carbons for Energy Storage. *Nat. Mater.* **2009**, *8*, 872−875.

(15) Tsai, W.-Y.; Taberna, P.-L.; Simon, P. Electrochemical Quartz Crystal Microbalance (EQCM) Study of Ion Dynamics in Nanoporous Carbons. *J. Am. Chem. Soc.* **2014**, *136*, 8722−8728.

(16) Griffin, J. M.; Forse, A. C.; Tsai, W.-Y.; Taberna, P.-L.; Simon, P.; Grey, C. P. In Situ NMR and Electrochemical Quartz Crystal Microbalance Techniques Reveal the Structure of the Electrical Double Layer in Supercapacitors. *Nat. Mater.* **2015**, *14*, 812−819.

(17) Zhou, J.; Li, Z.; Xing, W.; Shen, H.; Bi, X.; Zhu, T.; Qiu, Z.; Zhuo, S. A New Approach to Tuning Carbon Ultramicropore Size at Sub-Angstrom Level for Maximizing Specific Capacitance and CO_2 Uptake. *Adv. Funct. Mater.* **2016**, *26*, 7955−7964.

(18) Salanne, M.; Rotenberg, B.; Naoi, K.; Kaneko, K.; Taberna, P.-L.; Grey, C. P.; Dunn, B.; Simon, P. Efficient Storage Mechanisms for Building Better Supercapacitors. *Nat. Energy* **2016**, *1*, 16070.

(19) Kondrat, S.; Pérez, C. R.; Presser, V.; Gogotsi, Y.; Kornyshev, A. A. Effect of Pore Size and Its Dispersity on the Energy Storage in Nanoporous Supercapacitors. *Energy Environ. Sci.* **2012**, *5*, 6474−6479.

(20) Palmer, J. C.; Llobet, A.; Yeon, S.-H.; Fischer, J. E.; Shi, Y.; Gogotsi, Y.; Gubbins, K. E. Modeling the Structural Evolution of Carbide-Derived Carbons Using Quenched Molecular Dynamics. *Carbon* **2010**, *48*, 1116−1123.

(21) Boukhalfa, S.; Gordon, D.; He, L.; Melnichenko, Y. B.; Nitta, N.; Magasinski, A.; Yushin, G. In Situ Small Angle Neutron Scattering Revealing Ion Sorption in Microporous Carbon Electrical Double Layer Capacitors. *ACS Nano* **2014**, *8*, 2495−2503.

(22) Bañuelos, J. L.; Feng, G.; Fulvio, P. F.; Li, S.; Rother, G.; Dai, S.; Cummings, P. T.; Wesolowski, D. J. Densification of Ionic Liquid Molecules within a Hierarchical Nanoporous Carbon Structure Revealed by Small-Angle Scattering and Molecular Dynamics Simulation. *Chem. Mater.* **2014**, *26*, 1144−1153.

(23) Raccichini, R.; Varzi, A.; Passerini, S.; Scrosati, B. The Role of Graphene for Electrochemical Energy Storage. *Nat. Mater.* **2015**, *14*, 271−279.

(24) Stoller, M. D.; Park, S.; Zhu, Y.; An, J.; Ruoff, R. S. Graphene-Based Ultracapacitors. *Nano Lett.* **2008**, *8*, 3498−3502.

(25) Li, C.; Shi, G. Functional Gels Based on Chemically Modified Graphenes. *Adv. Mater.* **2014**, *26*, 3992−4012.

(26) Inagaki, M.; Kang, F. *Materials Science and Engineering of Carbon*, 1st ed.; Butterworth-Heinemann, 2016.

(27) Galhena, D. T. L.; Bayer, B. C.; Hofmann, S.; Amaratunga, G. A. J. Understanding Capacitance Variation in Sub-Nanometer Pores by in Situ Tuning of Interlayer Constrictions. *ACS Nano* **2016**, *10*, 747−754.

(28) Lee, K.; Yoon, Y.; Cho, Y.; Lee, S. M.; Shin, Y.; Lee, H.; Lee, H. Tunable Sub-Nanopores of Graphene Flake Interlayers with Conductive Molecular Linkers for Supercapacitors. *ACS Nano* **2016**, *10*, 6799−6807.

(29) Yuan, K.; Xu, Y.; Uihlein, J.; Brunklaus, G.; Shi, L.; Heiderhoff, R.; Que, M.; Forster, M.; Chassé, T.; Pichler, T. T.; et al. Straightforward Generation of Pillared, Microporous Graphene Frameworks for Use in Supercapacitors. *Adv. Mater.* **2015**, *27*, 6714−6721.

(30) Stankovich, S.; Dikin, D. A.; Piner, R. D.; Kohlhaas, K. A.; Kleinhammes, A.; Jia, Y.; Wu, Y.; Nguyen, S. T.; Ruoff, R. S. Synthesis of Graphene-Based Nanosheets via Chemical Reduction of Exfoliated Graphite Oxide. *Carbon* **2007**, *45*, 1558−1565.

(31) Dreyer, D. R.; Park, S.; Bielawski, C. W.; Ruoff, R. S. The Chemistry of Graphene Oxide. *Chem. Soc. Rev.* **2010**, *39*, 228−240.

(32) Herrera-Alonso, M.; Abdala, A. A.; McAllister, M. J.; Aksay, I. A.; Prud'homme, R. K. Intercalation and Stitching of Graphite Oxide with Diaminoalkanes. *Langmuir* **2007**, *23*, 10644−10649.

(33) Hung, W.-S.; Tsou, C.-H.; De Guzman, M.; An, Q.-F.; Liu, Y.-L.; Zhang, Y.-M.; Hu, C.-C.; Lee, K.-R.; Lai, J.-Y. Cross-Linking with Diamine Monomers To Prepare Composite Graphene Oxide-Framework Membranes with Varying d-Spacing. *Chem. Mater.* **2014**, *26*, 2983−2990.

(34) Li, D.; Muller, M. B.; Gilje, S.; Kaner, R. B.; Wallace, G. G. Processable Aqueous Dispersions of Graphene Nanosheets. *Nat. Nanotechnol.* **2008**, *3*, 101−105.

(35) Banda, H.; Aradilla, D.; Benayad, A.; Chenavier, Y.; Daffos, B.; Dubois, L.; Duclairoir, F. One-Step Synthesis of Highly Reduced Graphene Hydrogels for High Power Supercapacitor Applications. *J. Power Sources* **2017**, *360*, 538−547.

(36) Brunauer, S.; Emmett, P. H.; Teller, E. Adsorption of Gases in Multimolecular Layers. *J. Am. Chem. Soc.* **1938**, *60*, 309−319.

(37) Jagiello, J.; Olivier, J. P. 2D-NLDFT Adsorption Models for Carbon Slit-Shaped Pores with Surface Energetical Heterogeneity and Geometrical Corrugation. *Carbon* **2013**, *55*, 70−80.

(38) Srinivas, G.; Burress, J. W.; Ford, J.; Yildirim, T. Porous Graphene Oxide Frameworks: Synthesis and Gas Sorption Properties. *J. Mater. Chem.* **2011**, *21*, 11323−11329.

(39) Ue, M. Mobility and Ionic Association of Lithium and Quaternary Ammonium Salts in Propylene Carbonate and Γ-Butyrolactone. *J. Electrochem. Soc.* **1994**, *141*, 3336−3342.

(40) Zhang, L.; Zhang, F.; Yang, X.; Long, G.; Wu, Y.; Zhang, T.; Leng, K.; Huang, Y.; Ma, Y.; Yu, A.; Chen, Y. Porous 3D Graphene-Based Bulk Materials with Exceptional High Surface Area and Excellent Conductivity for Supercapacitors. *Sci. Rep.* **2013**, *3*, 1408.

(41) Zhu, Y.; Murali, S.; Stoller, M. D.; Ganesh, K. J.; Cai, W.; Ferreira, P. J.; Pirkle, A.; Wallace, R. M.; Cychosz, K. A.; Thommes, M.; et al. Carbon-Based Supercapacitors Produced by Activation of Graphene. *Science* **2011**, *332*, 1537−1541.

(42) Hummers, W. S.; Offeman, R. E. Preparation of Graphitic Oxide. *J. Am. Chem. Soc.* **1958**, *80*, 1339−1339.

(43) Ashok Kumar, N.; Gambarelli, S.; Duclairoir, F.; Bidan, G.; Dubois, L. Synthesis of High Quality Reduced Graphene Oxide Nanosheets Free of Paramagnetic Metallic Impurities. *J. Mater. Chem. A* **2013**, *1*, 2789−2794.

Supporting Information

Ion Sieving Effects in Chemically Tuned Pillared Graphene Materials for Electrochemical Capacitors

Harish Banda,[†*] Barbara Daffos, [¶,‡] Sandy Périé,[†] Yves Chenavier,[†] Lionel Dubois,[†] David Aradilla,[†] Stéphanie Pouget,[±] Patrice Simon, [¶,‡] Olivier Crosnier,[§] Pierre-Louis Taberna[¶,‡] and Florence Duclairoir[†*]

Characterization techniques

The thermogravimetric analysis (TGA) of all samples were performed with Setaram TGA 92 at a heating ramp rate of 5°C/min from 30°C to 800°C under N_2 atmosphere. The crystallographic structures of the materials were determined by a wide-angle X-ray diffraction (XRD) system on a Panalytical X'pert PRO X-ray diffractometer using a Co Kα radiation source (λ=1.79 Å). X-ray photoelectron spectroscopy (XPS) analyses were performed using a PHI Versa Probe II spectrometer with a monochromatized Al Kα X-ray source (1486.6 eV) focalized to a spot of 100 μm and with an electron take-off angle of θ = 45°. Survey spectra of the photo-emitted electrons were recorded with a pass energy of 117 eV and the high-resolution spectra with a pass energy of 23.5 eV. The deconvolution of C 1s and N 1s core-level spectra was performed by fitting the individual components at values obtained from earlier reports by using Casa XPS software[1]. Spectra were fitted into Gaussian-Lorentzian (30) shaped curves with full width at half maximum values kept under 1.5 in all cases. The morphology of the materials was characterized using a Zeiss Ultra 55 electron microscope at an accelerating voltage of 5 kV. Porosity characteristics were calculated from N_2 sorption isotherms measured at 77 K with Micromeritics ASAP 3020 porosimeter. Prior to the analysis samples have been subjected to a degazing at 100°C for 24h. The adsorption isotherms were obtained and the specific surface area and the pore size distributions (PSD) were calculated by assuming a graphene-based structural framework and using a 2D non-local density functional theory (NLDFT) treatment of the fluid density in the pores which are considered as energetically heterogeneous[2].

Electrochemical analysis

The synthesized materials were tested in a three-electrode supercapacitor configuration with porous carbon (YP50) as counter, silver wire as reference electrodes and a 25 μm thick cellulose sheet as a separator. Large porous carbon electrodes with excess weight were used to counter the charges and ensure distinct responses from the working electrodes. A custom-built Swagelok type cell was used to assemble the cell components. The working electrodes were fabricated as a slurry by mixing active materials, polyvinylidene fluoride (PVDF) and acetylene black carbon in a ratio of 80:10:10 using N-methyl-2-pyrrolidone and are coated onto 0.5 cm² stainless steel disks. The as prepared electrodes were dried at 65°C in air for 3 h prior to drying under vacuum at 120°C overnight. The dried electrodes were noted to weigh 1 - 1.5 mg resulting in loading densities of 2-3 mg/cm². 1M tetralkylammonium tetrafluoroborate

1

(TAABF$_4$) salt solutions in anhydrous acetonitrile with varying cations; ethyl (TEABF$_4$), propyl (TPABF$_4$), butyl (TBABF$_4$) and hexyl (THABF$_4$), are used as electrolytes. The performances of SC were evaluated using cyclic voltammetry (CV) at various scan rates. A multichannel VMP3 potentiostat/galvanostat with EC-Lab software (Biologic) was used for all electrochemical techniques. CV measurements were performed between - 1 to 1 V vs. Ag. at scan rates of 10, 20 and 50 mV s^{-1}. The gravimetric capacitances (C) were derived from CV curves using the equation $C = (\int I(v).dv) /(m(dv/dt).V)$, where $\int I(v).dv$ is the total area under the curve in the potential window, dv/dt is the scan rate, m is the mass of the active material in the working electrode and V is the total potential window.

Material	TGA Analyses			XPS - Elemental Composition			XRD Analyses		BET Analyses
	Wt. loss (%)[a]	Wt. loss with RGO as Ref.[b]	Grafting density[c]	C %	O %	N %	d (Å) G	d (Å) CL	Specific Surface Area (m²/g)
GO	43	-	-	74.7	25.3	-	-	7.6	
RGO	14	-	-	91.2	4.5	4.3	3.7	-	330
5 RP	31	17	0.16	86.5	8.0	5.3	3.9	7.8	138
6 RP	33	19	0.15	86.8	7.6	5.4	3.9	8.0	130
8 RP	37	23	0.16	86.8	7.6	5.5	4.0	8.6	108

Table S1. Thermal gravimetric weight loss values, elemental composition values from X-ray photoelectron spectroscopy and d-spacing obtained from X-ray diffraction spectra for the synthesized materials. The grafting densities of the diamines in different RPs were calculated by normalizing TGA weight losses with respect to RGO and dividing by the respective diamine molecular weights. Weight losses at 800°C[a] were used for this calculation assuming that all the diamines in RPs would be degraded by this temperature. [b]Weight losses in RPs normalized with RGO as baseline. [c]Adjusted weight loss of RPs were divided by the respective diamine molecular weights for a comparison of the amounts of diamine.
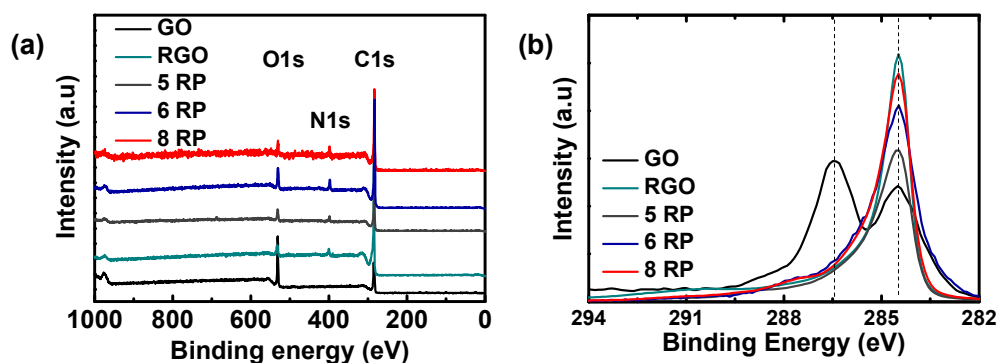
Figure S1. X-ray photoelectron (a) survey scans and (b) C 1s high-resolution spectra of GO, RGO and RPs. The spectra indicate presence of C, N and O elements in the materials with GO showing significantly higher O intensities compared to others.
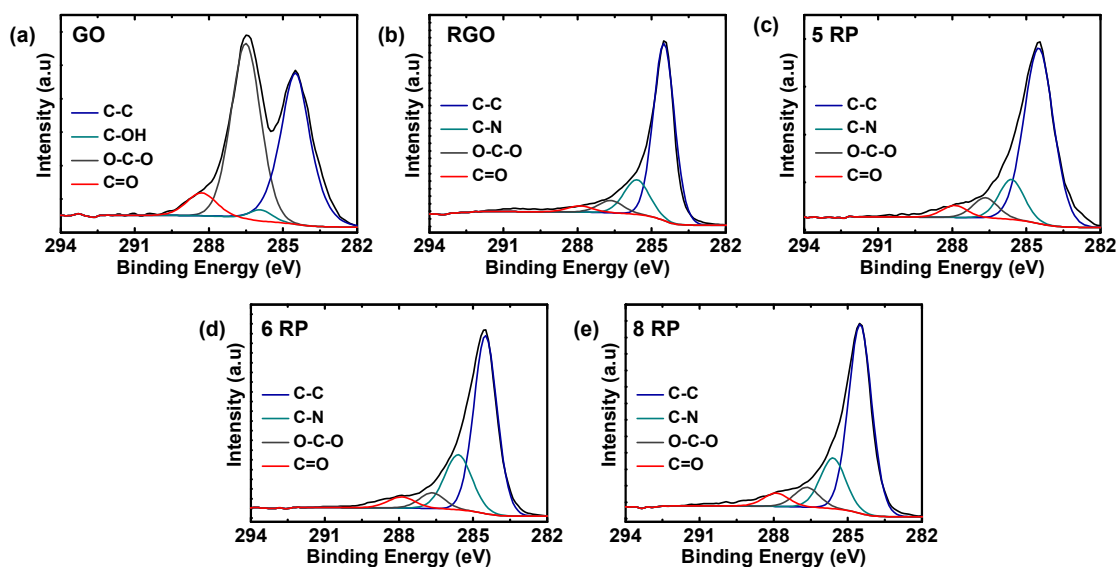

Figure S2. C 1s high-resolution X-ray photoelectron spectra of (a) GO, (b) RGO, (c) 5 RP, (d) 6 RP and (e) 8 RPs. The signals from C atoms in different chemical environments are deconvoluted as C-C/C=C (284.5 eV), C-N (285.6 eV), C-OH (285.9 eV), epoxy/alkoxy (286.5 eV) and carbonyl groups (288.3 eV).

3
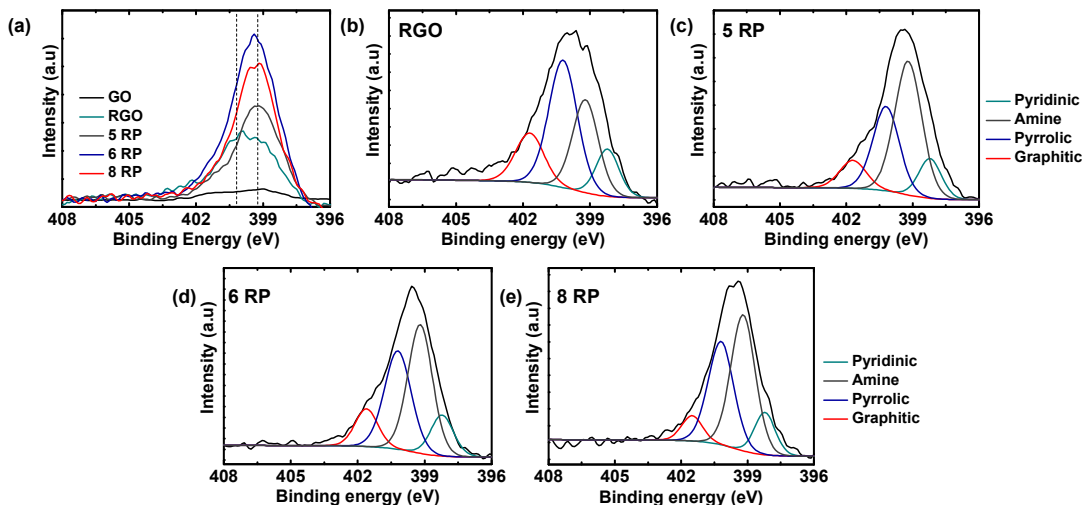
Figure S3. (a) N 1s high-resolution X-ray photoelectron spectra of GO, RGO and RPs. Deconvolutions of high resolution N 1s signal into pyridinic (398.2 eV), amine (399.2 eV), pyrrolic (400.2 eV), and graphitic (401.5 eV) components for (b) RGO, (c) 5 RP (d) 6 RP and (e) 8 RP.
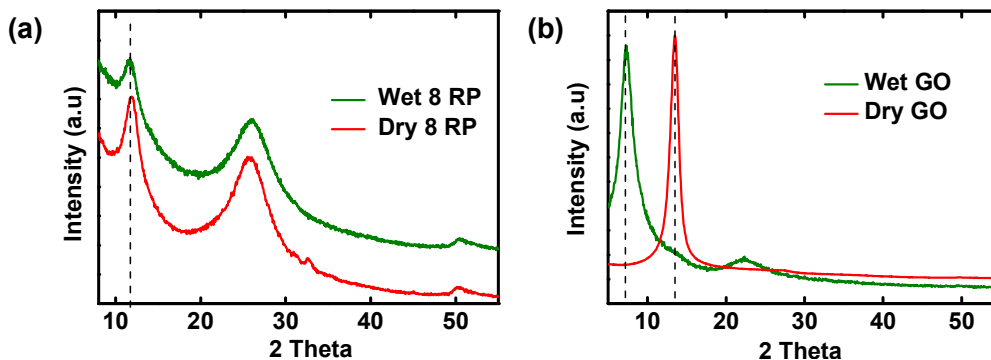

Figure S4. (a) X-Ray diffraction spectra of 8 RP before and after soaking in 80% ethanol-water solution for overnight, (b) X-Ray diffraction spectra of GO before and after soaking in 80% ethanol-water solution for 5 minutes. Even after soaking overnight in ethanol-water solution, XRD pattern of 8 RP remains unchanged confirming that the presence of covalent crosslinks between the sheets. Visible swelling and shift in XRD peak positions is seen in GO after just few minutes in solvent and thus highlighting the lack of cross-linking.
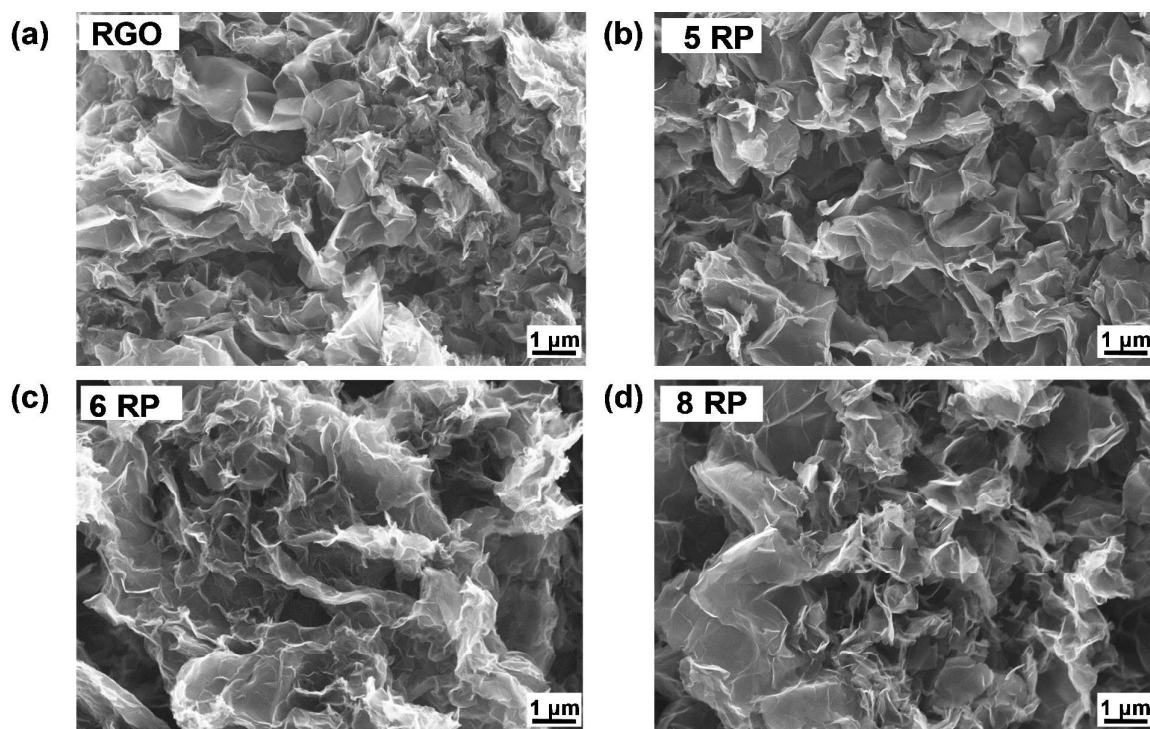
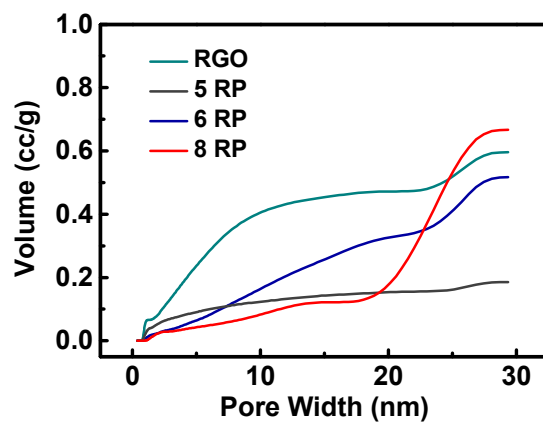Figure S5. Scanning electron microscopy images of (a) RGO, (b) 5 RP, (c) 6 RP and (d) 8 RP.

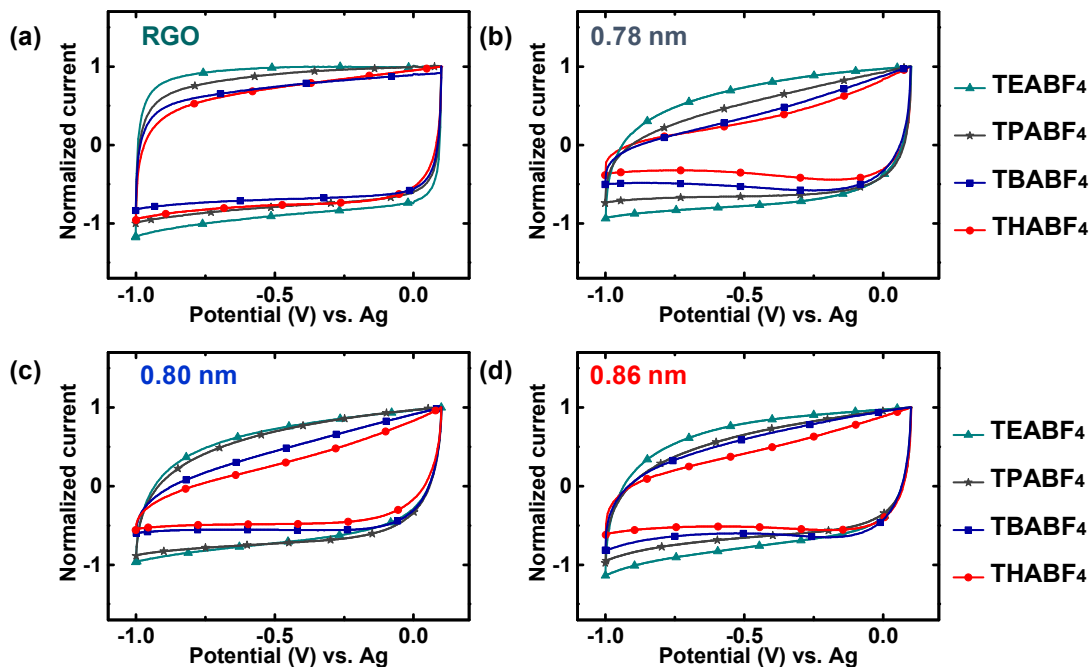Figure S6. Cumulative porous volumes of the synthesized materials.

Figure S7. Normalized CVs of (a) RGO (b) 5 RP (d = 0.78 nm), (c) 6 RP (d = 0.80 nm) and (d) 8 RP (d = 0.86 nm) obtained using various 1 M TAABF$_4$ / acetonitrile electrolytes at a scan rate of 20 mV s^{-1} in the voltage range of -1.0 V to 0.1 V vs. Ag. RGO lacks nanopores or cross-linked interlayer galleries and hence does not show any specific limitation to TAA$^+$ cations.
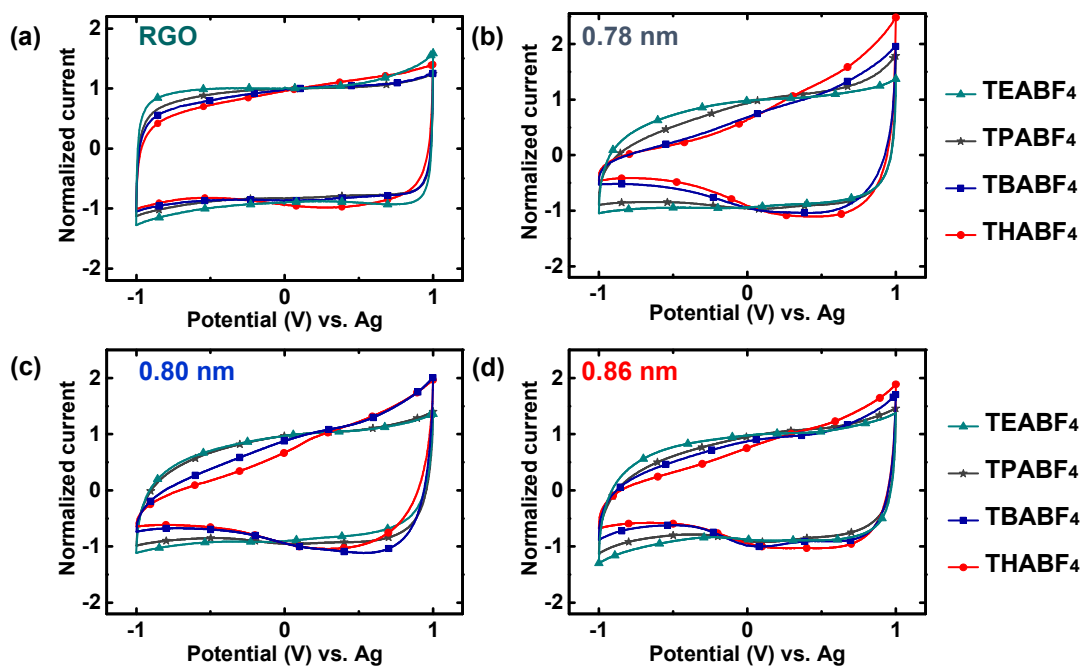
Figure S8. Normalized CVs of (a) RGO (b) 5 RP (d = 0.78 nm), (c) 6 RP (d = 0.80 nm) and (d) 8 RP (d = 0.86 nm) obtained using various 1 M TAABF$_4$ / acetonitrile electrolytes at a scan rate of 20 mV s^{-1} in the voltage range of -1.0 V to 1.0 V vs. Ag. RGO lacks pores or inter layer galleries spacing below 1 nm and hence doesn't show any specific limitation to TAA$^+$ cations.
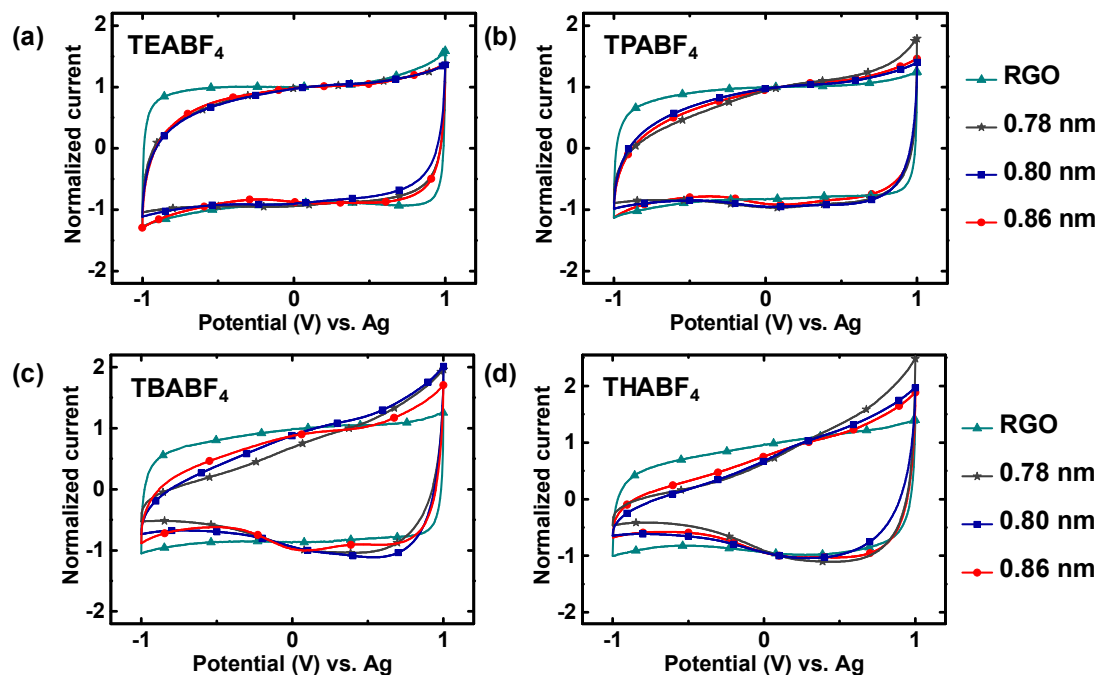
Figure S9. Normalized CVs of RGO and RPs obtained at scan rates of 20 mV s^{-1} in the voltage range of -1.0 V to 1.0 V vs. Ag using 1 M solutions of (a) TEABF$_4$ (Φ= 0.68 nm), (b) TPABF$_4$ (Φ= 0.76 nm), (c) TBABF$_4$ (Φ= 0.82 nm), and (d) THABF$_4$ (Φ= 0.95 nm) in acetonitrile as electrolytes.
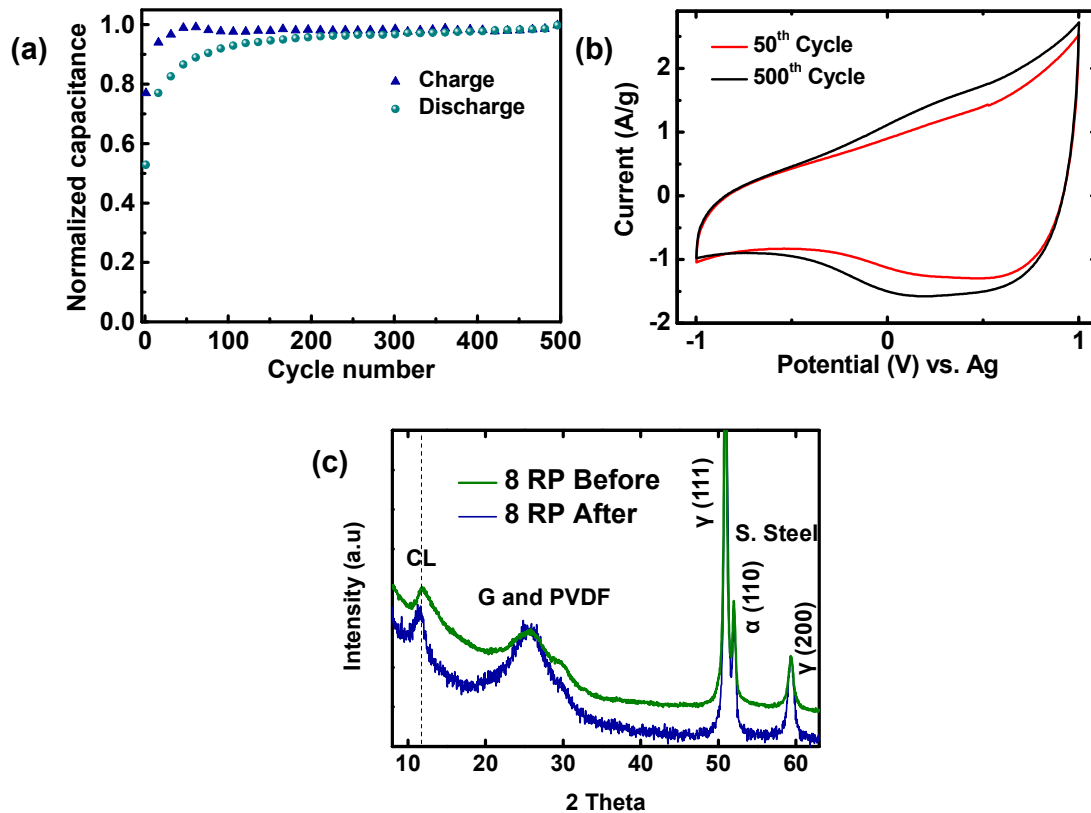
Figure S10. (a) Normalized charge-discharge capacitances of 8RP obtained from CVs in 1M THABF$_4$/AN at 50 mV/s scan rate in the potential range of -1 to 1 V vs. Ag over 500 cycles. (b) CV curves for the 50th and the 500th cycles and (c) Ex-situ XRD patterns of 8 RP electrode before and after 500 CV cycles at 50 mV/s scan rate in the potential range of -1 to 1 V vs. Ag. Cross-linking (CL) peak is retained even after 500 CV cycles. In addition, peaks corresponding to PVDF binder and stainless steel current collector are also seen.
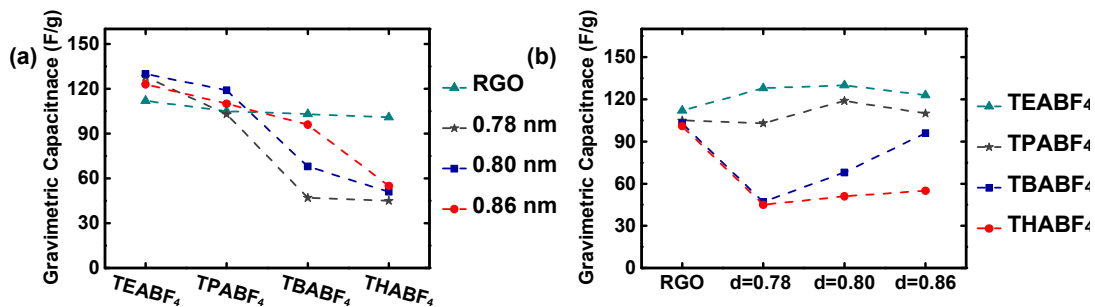

Figure S11. Specific capacitances are calculated from CVs at 20 mV s^{-1} for the cells tested in the voltage range of -1.0 V to 1.0 V vs. Ag. Values are shown with (a) variation in the electrolyte and (b) change in the material.

Material	Electrolyte	Specific Capacitance (F/g) (Conditions)	Reference
Commercial activated carbon	-	80~120	3
Carbide derived carbon	EMIMTFSI	160 (0.3 A/g)	4
Chemically reduced graphene	TEABF$_4$/AN	99 (1.3 A/g)	5
Activated graphene	EMIMBF$_4$	231 (1 A/g)	6
a-MEGO	BMIMIBF$_4$/AN	165 (1 A/g)	7
5 RP (This work)	**TEABF$_4$/AN**	**130 (20 mV s^{-1})** **154 (1 A/g)**	-

Table S2. Comparison between the performances of various carbons found in the literature.

References:
(1) Stankovich, S.; Dikin, D. A.; Piner, R. D.; Kohlhaas, K. A.; Kleinhammes, A.; Jia, Y.; Wu, Y.; Nguyen, S. T.; Ruoff, R. S. Synthesis of Graphene-Based Nanosheets via Chemical Reduction of Exfoliated Graphite Oxide. *Carbon* **2007**, *45* (7), 1558–1565.
(2) Jagiello, J.; Olivier, J. P. 2D-NLDFT Adsorption Models for Carbon Slit-Shaped Pores with Surface Energetical Heterogeneity and Geometrical Corrugation. *Carbon* **2013**, *55* (Supplement C), 70–80.
(3) Burke, A. R&D Considerations for the Performance and Application of Electrochemical Capacitors. *Electrochimica Acta* **2007**, *53* (3), 1083–1091.
(4) Largeot, C.; Portet, C.; Chmiola, J.; Taberna, P.-L.; Gogotsi, Y.; Simon, P. Relation between the Ion Size and Pore Size for an Electric Double-Layer Capacitor. *J. Am. Chem. Soc.* **2008**, *130* (9), 2730–2731.
(5) Stoller, M. D.; Park, S.; Zhu, Y.; An, J.; Ruoff, R. S. Graphene-Based Ultracapacitors. *Nano Lett.* **2008**, *8* (10), 3498–3502.
(6) Zhang, L.; Zhang, F.; Yang, X.; Long, G.; Wu, Y.; Zhang, T.; Leng, K.; Huang, Y.; Ma, Y.; Yu, A.; et al. Porous 3D Graphene-Based Bulk Materials with Exceptional High Surface Area and Excellent Conductivity for Supercapacitors. *Sci. Rep.* **2013**, *3*, 1408.
(7) Zhu, Y.; Murali, S.; Stoller, M. D.; Ganesh, K. J.; Cai, W.; Ferreira, P. J.; Pirkle, A.; Wallace, R. M.; Cychosz, K. A.; Thommes, M.; et al. Carbon-Based Supercapacitors Produced by Activation of Graphene. *Science* **2011**, *332* (6037), 1537–1541.